

Modeling and Simulation of Membrane-Based Dehumidification and Energy Recovery Process

Zhiming Gao, PhD

Omar Abdelaziz, PhD
Member ASHRAE

Ming Qu, PhD
Member ASHRAE

ABSTRACT HEADING

This paper introduces a first-order physics-based model that accounts for the fundamental heat and mass transfer between a humid-air vapor stream on the feed side to another flow stream on the permeate side. The model comprises a few optional submodels for membrane mass transport, and adopts a segment-by-segment method for discretizing heat and mass transfer governing equations for flow streams on the feed and permeate sides. The model is able to simulate both dehumidifiers and energy recovery ventilators in parallel-flow, cross-flow, and counter-flow configurations. The predicted results compares reasonably well with the measurements. The model and C++ open-source codes are expected to become a fundamental tool for the analysis of membrane-based dehumidification in the future.

INTRODUCTION

Compared to typical dehumidification technologies like desiccant and vapor-compression cycle dehumidification (Abdelaziz 2015, Gao 2010, Gao et al. 2005), membrane-based dehumidification is a promising solution for building applications due to its low cost and very limited energy consumption. However, its HVAC application is still at an early stage of development (Wood 2014). Developing an efficient open-source code simulation tool is important for elevating the optimization and application of such technologies, particularly in heating, ventilation, and air conditioning devices.

Many modeling studies have been carried out to support the implementation and market penetration of membrane-based devices in building and HVAC applications (Ding et al. 2002, Zhang et al. 2008, Min et al. 2010, Zaw et al. 2013). The most common modeling approach is based on one-dimensional finite difference methodology (Niu et al. 2001, Zaw et al. 2013). Some 2D and 3D Computational fluid dynamics simulations for membrane and flow channels were also reported, but did not demonstrate significant improvement compared to those low-order physical-constant models (Zhang et al. 2010, Yu et al. 2011, Zaw et al. 2013). This is not surprising because of the μm -level membrane thickness and millimeter-level channel height compared to significantly dimensions in the flow streams. Some researchers also used NTU-effectiveness approaches or electrical circuit analogy of transport resistances to investigate either heat or mass transfer (Qtaishata et al. 2008, Bui et al. 2010).

The adopted models for membrane mass transport are usually based on water vapor diffusivity (Zhang et al. 2010, Zaw et al. 2013), mass transfer resistance with vapor sorption correction (Niu et al. 2001, Zhang et al. 2008, Min et al. 2010), or constant coefficients available from measurements (Yu et al. 2011). These empirical mass transport models are not able to account for material physical properties, driving forces, and membrane microstructure involved in a porous membrane; thus these models are hardly able to support membrane design and optimization. On the other hand, some modeling efforts adopted membrane mass transport methodologies based on dusty gas models (Mason et

al. 1983, Ding et al. 2002), which are capable of accounting for transportation mechanism (like Knudsen-diffusion, Molecular-diffusion, and Poiseuille-flow) within smaller porous materials. These models rationally describe hydrophobic microporous membranes and their driving force under a thermally driven process or vapor pressure difference. Such models have been widely used in membrane distillation (Ding et al. 2002, Qtaishata et al. 2008), but have not been utilized in membraned-based HVAC applications to our knowledge. Thus the usage of such membrane microstructure modeling is interesting to account for complex membrane materials used in HVAC device, and is also important to identify their accuracy vs. empirical models based on measurements.

For interfacial thermal transport between a membrane and flow streams on the feed and permeate sides, the correlation of Nusselt (Nu) and Sherwood (Sh) numbers are frequently used. Fully developed laminar flow is typically considered in the studies. However, these models generally ignore the thermal effect of mass flux through membranes (Niu et al. 2001, Zhang et al. 2008, Min et al. 2010, Yu et al. 2011). Moreover, the reported models do not account for membrane deflection on heat and mass transfer. Membrane deflection can significantly influence the performance of membrane-based air dehumidification and energy recovery ventilation (Larson et al. 2008). Consequently, there still lacks an efficient and physical-constant simulation tool which adequately accounts for the fundamental heat and mass transfer between a humid-air vapor stream on the feed side to flow streams on the permeate side.

This paper reports on the development of an open-source code which enables to model and simulate a membrane-based air-to-air or air-to-vapor device. A first-order physical-constant model was developed to account for the fundamental heat and mass transfer processes involved. In the proposed model, a segment-by-segment approach is used to discretize heat and mass transfer governing equations which include the impact of thermal effects of mass flux through membranes and membrane deflection. The model also includes various membrane mass transfer submodels, which are capable of comparing their predictions and identifying their gaps. The reported model is capable of simulating dehumidifiers and energy recovery ventilators with various flow configurations. The model has been validated with both isothermal and non-isothermal measurements. In the following model and simulations, we focus on the membranes with the property of high-selective water vapor transfer.

METHODOLOGY AND ASSUMPTIONS

Membrane Mass Transport

In a membrane with high-selective water vapor transfer, the mass transfer of air vapor on the feed side to a vacuum or low vapor-pressure air stream on the permeate side typically occur in three steps: adsorption at the feed side of the membrane; vapor diffusion through the membrane; and desorption at the permeate side of the membrane. The vapor diffusion rate through the membrane is equivalent to the adsorption rate and desorption rate under the steady state conditions. Also, the permeated rate of water vapor through a membrane is typically proportional to the vapor partial pressure difference between two sides of the membrane. Thus, the permeated water vapor flux can be calculated via Eq. 1. Air permeation through the membrane is not considered in the studies due to the properties of the selected membrane.

$$f_v = K_v (P_{f,v} - P_{p,v}) \quad (1)$$

where f_v is the permeated flux of water vapor; $P_{f,v}$ and $P_{p,v}$ are the partial vapor pressures on feed and permeate sides, respectively; K_v is the intrinsic membrane permeability coefficients of water vapor.

K_v is a vital material parameter which is used to characterize the mass transport performance of membranes. There are three key mass transport mechanisms in a porous membrane: Knudsen-diffusion, Molecular-diffusion, and Poiseuille-flow. Other mechanisms like thermal and surface diffusion, which are very limited, are neglected here. So K_v can be estimated via the combination of multiple mass transport mechanisms. Table 1 lists the various mechanisms that are available in our code. In the study, a microstructure model combined with Knudsen diffusion, molecular diffusion, and Poiseuille flow is adopted to account for mass transport through the membrane.

Table 1: Definition of K_v as a function of various mechanisms

Transport mechanism	Definition of K_v
Knudsen diffusion	$K_v = K_{Kd}$
Molecular diffusion	$K_v = K_{Md}$
Poiseuille flow	$K_v = K_{Pf}$
Knudsen diffusion -molecular diffusion	$K_v = K_{Kd}K_{Md}/(K_{Kd} + K_{Md})$
Knudsen diffusion -molecular diffusion-poiseuille flow	$K_v = K_{Kd}K_{Md}/(K_{Kd} + K_{Md}) + K_{Pf}$

The detailed coefficients of Knudsen-diffusion, Molecular-diffusion, and Poiseuille-flow are given by Eqs. 2-4.

$$\text{Knudsen-diffusion: } K_{Kd} = \frac{2}{3} \frac{r \varepsilon}{\tau \delta} \left(\frac{8M_v}{\pi R T_m} \right)^{0.5} \quad (2)$$

$$\text{Molecular-diffusion: } K_{Md} = \frac{\varepsilon}{\tau \delta} \frac{P_v D_v}{P_a} \left(\frac{M_v}{R T_m} \right) \quad (3)$$

$$\text{Poiseuille-flow: } K_{Pf} = \frac{1}{8} \frac{r^2 \varepsilon}{\tau \delta} \left(\frac{M_v P_v}{\mu R T_m} \right) \quad (4)$$

where ε , τ , r , and δ are the porosity, pore tortuosity, pore radius and thickness of the membrane; T_m is the membrane temperature; μ is the viscosity of humid air; P_v is the vapor pressure of the membrane; R is the universal gas constant; D_v is vapor diffusion in air.

To compare the microstructure mechanism model, we also developed a performance map of membrane permeability coefficient based on the laminar flow testing in a membrane sample made by an OEM (Dais 2015). Figure 1 shows the detailed performance map. The performance maps are used in Eq. 1 to compare with the microstructure model in predicting water vapor mass transfer through the membrane made by OEM (Dais 2015).

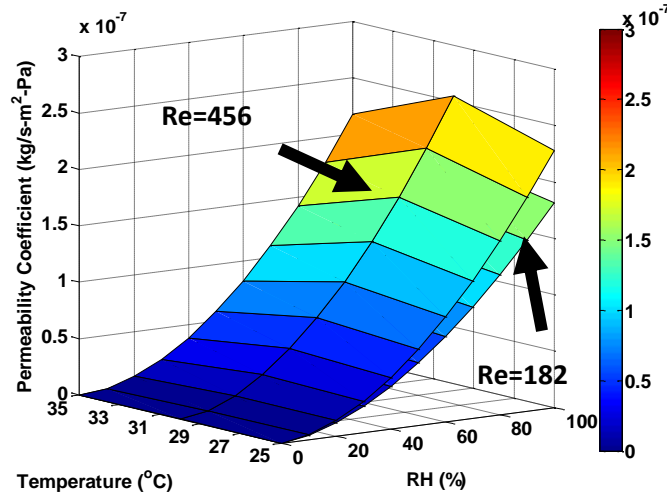


Figure 1 A performance map of membrane permeability coefficient at laminar flows. 1 kg/m²·pa = 1412.1 lb/ft²·psi.

Heat and Mass Transport of Flow Streams

An example schematic of a membrane-based dehumidifier or ventilator is shown in Figure 2. The device incorporates a cubic core where the two flow streams (i.e. the feed-side and permeation-side streams) in thin, parallel membrane layers with a cross-flow arrangement. To assist the model setup, we assume: (1) heat and mass transfer are in steady state; (2) heat conduction and vapor diffusion in the two flow stream are negligible; (3) feed and permeation flows are distributed homogeneously in each feed and permeation channels, respectively, in a multi-membrane layer system; (4) vapor diffusion through membrane is in equilibrium with the adsorption and desorption rates on feed and permeate sides, respectively; (5) membrane deflection adjusts effective membrane surface for heat and mass transfer.

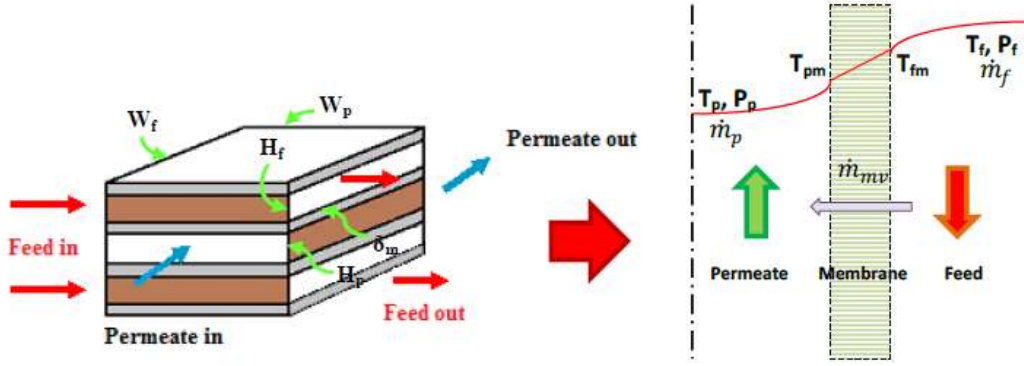


Figure 2 Schematic of a cross-flow membrane-based dehumidifier or ventilator.

Heat and mass transfer equations in the feed-side flow are described as Eqs. 5 and 6, respectively:

$$\dot{m}_f c_{pf} \frac{dT_f}{dx} + 2h_f W_f (T_f - T_{fm})\beta + 2f_v W_f (H_{f,v} - H_{fm,v})\beta = 0 \quad (5)$$

$$\frac{d\dot{m}_{f,v}}{dx} + 2f_v W_f \beta = 0 \quad (6)$$

Heat and mass transfer equations in the permeate-side flow are described as Eqs. 7 and 8, respectively:

$$\dot{m}_p c_{pp} \frac{dT_p}{dy} + 2h_p W_p (T_p - T_{pm})\beta + 2f_v W_p (H_{p,v} - H_{pm,v})\beta = 0 \quad (7)$$

$$\frac{d\dot{m}_{p,v}}{dy} - 2f_v W_p \beta = 0 \quad (8)$$

The boundary conditions of Eqs. 5-8 are given, respectively, as $T_f = T_{f,i}$ at $x=0$; $T_p = T_{p,i}$ at $y=0$; $\dot{m}_{f,v} = \dot{m}_{f,i} RH_{f,i}/(1 + RH_{f,i})$ at $x=0$; $\dot{m}_{p,v} = \dot{m}_{p,i} RH_{p,i}/(1 + RH_{p,i})$ at $y=0$. In a case that the permeate side is connected to a vacuum pump to produce vacuum as a driving force for vapor permeation, $T_p = T_{f,i}$ and $\dot{m}_{p,v} = 0$ at $y=0$.

The interfacial heat transfer between membrane and either the feed-side or permeate-side flows is given by:

$$0 = h_f (T_f - T_{fm}) - \lambda_m \frac{dT_m}{dz} + f_v (H_{f,v} - H_{fm,v}) \quad (9)$$

$$0 = h_p (T_p - T_{pm}) + \lambda_m \frac{dT_m}{dz} + f_v (H_{p,v} - H_{pm,v}) \quad (10)$$

where T_f , T_p , T_{fm} and T_{pm} are the temperature of feed-side flow, permeation-side flow, and interfacial membrane at the feed-side and permeation-side, respectively; $H_{f,v}$, H_{fm} , H_{pm} , and $H_{p,v}$ are the vapor enthalpy of feed-side flow, membrane interface at the feed-side, membrane interface at the permeation-side, permeation-side flow, respectively; h_f and h_p are heat transfer coefficients on the feed and permeate sides, respectively, which are estimated using a constant Nu number in a fully laminar flow due to smaller channel height and longer channel depth; W_f and W_p are the width of feed and permeate channels, respectively; the x and y axes represent feed-side and permeation-side flow directions, respectively, with the z axis representing membrane thickness, respectively; $\dot{m}_{f,v}$ and $\dot{m}_{p,v}$ represent the vapor mass flow rate on the feed-side and permeate-side, respectively; λ_m is membrane thermal conductivity; δ is membrane thickness; β is a factor accounting for membrane deflection.

To simplify the governing equations, we adopted a segment-by-segment methodology, where these equations in each segment are discretized and expressed as $AX = B$. The generated matrices are solved via Gaussian Elimination to achieve $T_{f,o}$, T_{fm} , T_{pm} , and $T_{p,o}$. Then $T_{f,o}$ and $T_{p,o}$ are further considered to be input parameters as $T_{f,i}$ and $T_{p,i}$ in the next segment analysis until all the segments are solved. Meanwhile, the mass transfer equations (i.e. Eqs. 6 and 8) are discretized and solved directly. The C++ codes are developed and available at (MBMS 2016).

The proposed model is based on a cross-flow case. However, the parallel-flow and counter-flow cases are also developed with somewhat different due to flow direction alteration. For example, in a counter-flow case, an iteration

solving method is specifically established to achieve a solid numerical convergence between the assumed and predicted values. This paper does not detail moist air and vapor properties which are available in the codes.

RESULTS AND ANALYSES

Isothermal dehumidification validation

The adopted experimental data were conducted by the OEM in a large scale dehumidification module which was assembled using 59 slats with nearly 120 membrane layers and a total membrane area of approximately 117.33 ft² (10.9 m²). The length and width of each slat are 1.38 ft × 0.72 ft (0.42 m × 0.22 m) while the channel heights of feed and permeate sides are 0.05 in and 0.135 in (1.27 mm and 3.43 mm), respectively. The membrane thickness is 0.787e-6 in (20 μm). The dehumidification module is a cross-flow configuration. The module was tested with an air-to-vapor mode in a climate-controlled chamber (Dais 2015), which generated humid air and manages temperature, relative humidity, flow rate and pressure level on the feed side while a vacuum pump was used to pull water vapor vacuum on the permeate side. The flow rates on the feed side are around 154-162 cfm (4378-4582 L/min).

Figure 3(a) compares the predicted vapor dehumidification rate by using the microstructure model and performance map model with the measurements. Here the constant vacuum pressure was maintained through the entire permeate-side channel. In the microstructure model simulation, we adopted 9.84e-9 in (0.25 μm) for pore radius, 0.55 for porosity, and 3.43-6.86 for tortuosity. The observations show the microstructure model achieves less accuracy compared with the performance map model. Moreover, membrane properties can affect the results predicted by the microstructure modeling significantly. For example, as shown in Figure 3(a), the average absolute error between the simulation and measurement is 14% and 23%, respectively, for the tortuosity of 3.43 and 6.86. Thus, achieving accurate membrane properties is vital to the microstructure model.

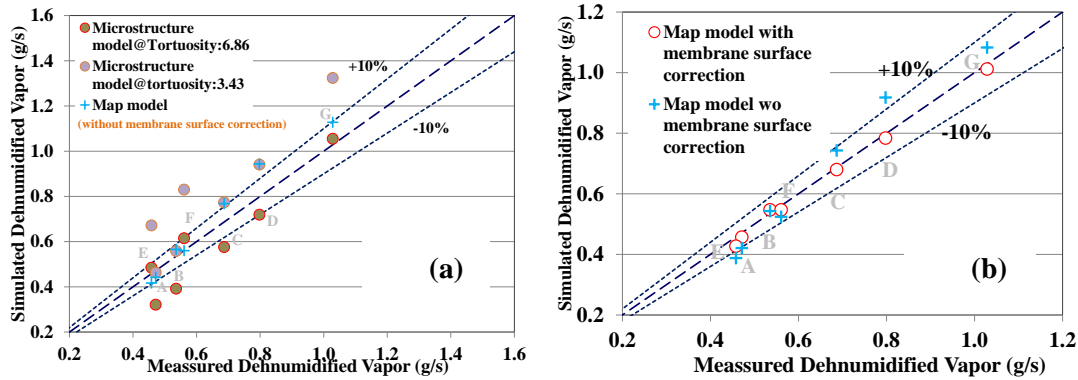


Figure 3 Comparison of the simulated vapor dehumidification rate using both the microstructure model and map model with the measurements. The flows operate in a cross-flow configuration. (a) shows all without membrane surface correction; (b) shows the impact of membrane surface correction. 1g/s=0.0022 lb/s.

Compared to the microstructure model, the performance map achieves a better accuracy. This is expected because the map data were measured directly from the tested membrane. However, the maximum predicted error for the simulated dehumidified vapor rate related to the performing map model is still up to 15%. The perfectly flat membrane surface was considered in the simulations. However, the membrane surface could experience significant deflection under the substantial vapor permeate process. To simplify the simulation accounting for this phenomenon, a factor was introduced to correct the surface deflection as described in the modeling section. Figure 3(b) shows the impact of membrane surface correction on the said results predicted by the map model. With the implementation of membrane surface correction, the maximum predicted error for the new simulated dehumidified vapor rate is reduced down to 6%. The mechanism of membrane surface deflection is complicated. We agree a constant value is just a preliminary effort. With the availability of comprehensive measured data in the future, a physical-constant model

accounting for such deflection mechanism should be developed.

Non-isothermal dehumidification validation

The data used for the non-isothermal dehumidification model validation are based on a literature (Zhang et al. 2008). The data were measured in three identical cross-flow exchangers with different membrane materials. The exchangers include 115 straight-through and parallel-plate channels for fresh air flow on the feed side and exhaust air flow on the permeate side, and each channel is 0.607 ft \times 0.607 ft (0.185 m \times 0.185 m) with 0.079 in (2.0 mm) height. These membrane materials used in the exchangers show different membrane thickness and physical properties. Thus the microstructure model was selected to account for membrane mass transfer process. To reasonably simplify the simulations of an air-to-air mode, we defined both sensible and latent effectiveness accounting for heat and mass transfer, shown in Eqs. 11.

$$\varepsilon_s = \frac{\dot{m}_f c_{pf} (T_{fa,i} - T_{fa,o})}{\min(\dot{m}_f c_{pf}, \dot{m}_p c_{pp}) (T_{fa,i} - T_{pa,i})} \quad \text{and} \quad \varepsilon_L = \frac{\dot{m}_f (\omega_{fa,i} - \omega_{fa,o})}{\min(\dot{m}_f, \dot{m}_p) (\omega_{fa,i} - \omega_{pa,i})} \quad (11)$$

Figure 4 compares the sensible and latent effectiveness simulated by the microstructure model with the measurements reported in (Zhang et al. 2008). Nu number used in the analysis is 7.54 based on the ratio of flow channel width to channel height (Incropera et al. 1996). The results show that the microstructure model can achieves 2.2% and 5.0% of average absolute errors in sensible and latent effectiveness, respectively. Their maximum errors for sensible and latent effectiveness are 5% and 18%, respectively. The proposed model is capable of providing meaningful insight about the membrane-based ventilation and dehumidification process, particularly on the impact of different membrane thickness and properties on the effectivenesses. In the simulations, the correcting factor for membrane deflection is considered as unity, representing a perfect flat-surface membrane.

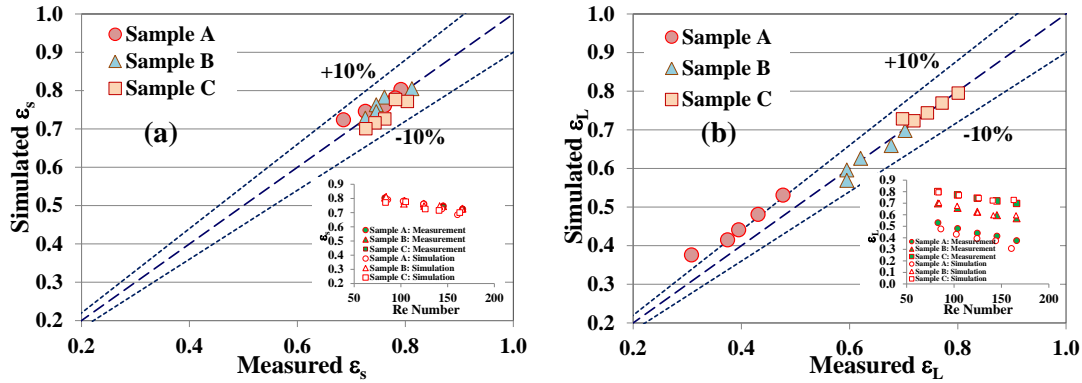


Figure 4 Comparison of the simulated sensible (a) and latent (b) effectiveness using the microstructure model with the measurements. Re number is based on feed-side air flows. The flow exchanger is a cross-flow configuration.

Case study

The model was further utilized to characterize impact of various flow configuration, flow stream conditions, and membrane surface deflection on air-to-air ventilation and dehumidification performance using the microstructure model. The considered flow configurations include parallel-flow, counter-flow and cross-flow. The studied flow stream conditions involve in various Reynolds number, feed-side temperature and humidity. The selected membrane material is the sample used in the section of non-isothermal dehumidification validation. The inlet fresh air temperature and humidity are 95 °F (35 °C) and 59% RH, respectively, while the exhaust air temperature and humidity are 80.6 °F (27 °C) and 54% RH, respectively. Figure 5 shows the impact of Reynolds number and membrane surface deflection factor on the performance of energy recovery and dehumidification with various flow configurations. The observations show that the counter-flow configuration achieves the best sensible and latent effectiveness, following by the cross-flow and parallel flow configurations. At Re=104, the parallel-flow configuration has significantly lower

effectiveness than the cross-flow and counter-flow configurations. However, at $Re=520$, the effectiveness advantage of the cross-flow and counter-flow configurations still exists, but is much less. The observations in Figure 5 further show that the impact of a given membrane surface deflection factor could be more significant at higher Re number than the cases at lower Re number. For example, A surface deflection factor of 0.65 could degrade the sensible and latent effectiveness by 5% and 10% respectively at $Re=104$, but reduce 10% and 20%, respectively, at $Re=520$. The combination of high flow rate and surface deflection can diminish the performance advantage of the cross-flow and counter-flow configurations significantly.

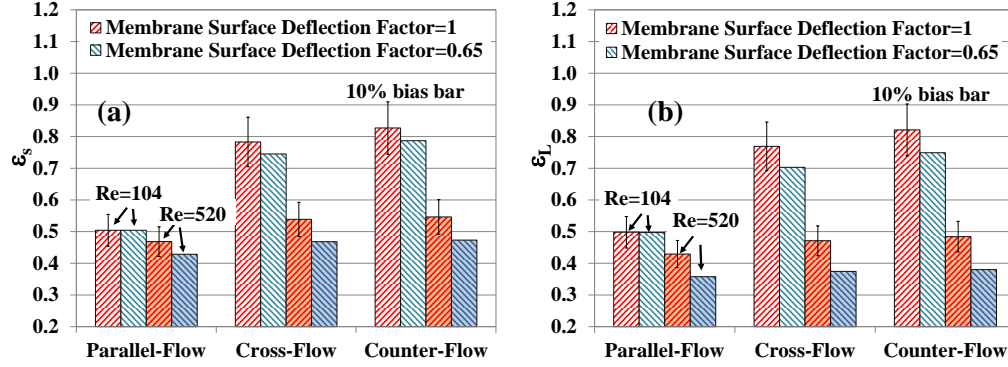


Figure 5 Effect of Re number and membrane surface deflection on the simulated sensible and latent effectiveness of various flow exchanger configurations. (a) Sensible effectiveness; (b) Latent effectiveness.

Figure 6 shows an example of the impact of Reynolds number and membrane surface deflection on the profiles of permeated vapor rate in a crossflow configuration. The results show that higher Re number leads to better permeated vapor rate in spite of less latent effectiveness shown in Figure 5. This is actually expected because higher Re number means significant feed air and vapor available in a flow stream. Meanwhile, the surface deflection also increases local permeated vapor rate per the unit of effective membrane surface, although the overall permeated vapor rate is reduced due to less effective mass transfer surface with the membrane surface deflection. Overall, the studied results demonstrate the current model is capable of providing substantial insight to membrane-based ventilation and dehumidification. We expect the model can assist membrane-based component analysis, design, and optimization.

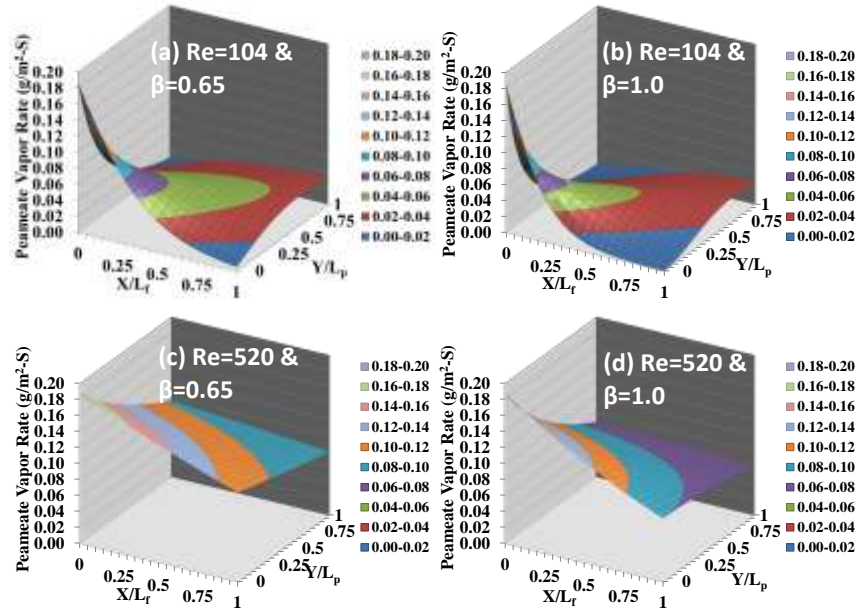


Figure 6 Effect of Re number and membrane surface deflection on the permeate vapor rate in a crossflow configuration. $1 \text{ g/m}^2 \cdot s = 2.05 \times 10^{-4} \text{ lb/ft}^2$.

CONCLUSION

A first-order physical-constant model has been developed to predict the performance of membrane-based device using a segment-by-segment method in accounting for the fundamental heat and mass transfer in a porous membrane. The model was validated with both isothermal and non-isothermal experimental data. The model has been used to compare various membrane mass transfer models, evaluate the impact of membrane microstructure features and membrane surface deflection factor, and investigate the performance of dehumidification and energy recovery exchangers under various operating conditions and flow configurations. The simulated results are expected to provide a reasonable trend for assisting membrane-based component analysis, design, and optimization.

ACKNOWLEDGMENTS

This project was sponsored by the US. Department of Energy's ARPA-E program. The authors would like to recognize Brian Johnson and Lacy Aliff of DAIS for their assistance and suggestions in our model validation.

REFERENCES

- Abdelaziz, O. 2015. Primary energy efficiency analysis of different separate sensible and latent cooling techniques. 2015 International Congress of Refrigeration, Yokohama, Japan.
- Bui, V., Vu, L., and M. Nguyen. 2010. Modelling the simultaneous heat and mass transfer of direct contact membrane distillation in hollow fibre modules. *Journal of Membrane Science* 353(1):85-93.
- Dais. 2015. Membrane dehumidification enabling alternative cooling strategies in humid environments. Final Scientific/Technical Report.
- Ding, Z., Ma, R., and A. Fane. 2002. A new model for mass transfer in direct contact, membrane distillation. *Desalination* 151:217-227.
- Gao, Z. 2010. The impact of thermostatic expansion valve heating on the performance of air-source heat pumps in heating mode. *Energy Conversion and Management* 51(4):732-739.
- Gao, Z., Mei V., and J. Tomlinson. 2005. Theoretical analysis of dehumidification process in a desiccant wheel, *Heat and Mass Transfer* 41(11):1033-1042.
- Incropera, F., and D. DeWitt. 1996. Introduction to heat transfer. 3rd edition, Wiley, NY.
- Larson, M., Besant, R., and C. Simonson. 2008. The effect of membrane deflections on flow rate in crossflow air-to-air exchangers. *HVAC&R Research* 14(2):275-288.
- Mason, E., and A. Malinauskas. 1983. Gas transport in porous media: the dusty-gas model, Chemical engineering monographs. Amsterdam: Elsevier Scientific Pub. Co.
- MBMS. 2016. https://github.com/MBMS/C-CODE_FOR_MEMBRANE_BASED_MODEL. Accessed October 4, 2016.
- Min, J., and M. Su. 2010. Performance analysis of a membrane-based energy recovery ventilator: effects of membrane spacing and thickness on the ventilator performance. *Applied Thermal Engineering* 30(8): 991-997.
- Niu, J., and L. Zhang. 2001. Membrane-based enthalpy exchanger: material considerations and clarification of moisture resistance. *Journal of Membrane Science* 189(2):179-191.
- Qtaishata, M., Matsuura, T., Kruczek, B., and M. Khayet. 2008. Heat and mass transfer analysis in direct contact membrane distillation. *Desalination* 219:272-292.
- Woods, J. 2014. Membrane processes for heating, ventilation, and air conditioning. *Renewable and Sustainable Energy Reviews* 33:290-304.
- Yu, H., Yang, X., Wang, R., and A. Fane. 2011. Numerical simulation of heat and mass transfer in direct membrane distillation in a hollow fiber module with laminar flow. *Journal of Membrane Science* 384:107-116.
- Zaw, K., Safizadeh, M., Luther, J., and K. Ng. 2013. Analysis of a membrane based air-dehumidification unit for air conditioning in tropical climates. *Applied Thermal Engineering* 59(1-2):370-379.
- Zhang, L., Liang, C., and L. Pei. 2008. Heat and moisture transfer in application scale parallel-plates enthalpy exchangers with novel membrane materials. *Journal of Membrane Science* 325:672-682.
- Zhang, L., Liang, C., and L. Pei. 2010. Conjugate heat and mass transfer in membrane-formed channels in all entry regions. *International Journal of Heat and Mass Transfer* 53(5):815-824.